Global stability of swept flow around a parabolic body: Features of the global spectrum

Christoph J. Mack, Peter J. Schmid

HAL Id: hal-00997979
https://polytechnique.hal.science/hal-00997979

Submitted on 5 Jun 2014

Global stability of swept flow around a parabolic body: features of the global spectrum

CHRISTOPH J. MACK[1,2]† AND PETER J. SCHMID[1]

[1]Laboratoire d'Hydrodynamique (LadHyX), CNRS-École Polytechnique, F-91128 Palaiseau, France

[2]Department of Numerical Mathematics, Universität der Bundeswehr (UniBw), D-85577 Munich, Germany

The global temporal stability of three-dimensional compressible flow about a yawed parabolic body of infinite span is investigated using an iterative eigenvalue technique in combination with direct numerical simulations. The computed global spectrum provides a comprehensive picture of the temporal perturbation dynamics of the flow, and a wide and rich variety of modes has been uncovered for the investigated parameter choices: stable and unstable boundary-layer modes, different types of stable and unstable acoustic modes, and stable wavepacket modes have been found. A parameter study varying the spanwise perturbation wavenumber and the sweep Reynolds number reproduced a preferred spanwise length scale and a critical Reynolds number for a boundary-layer or acoustic instability. Convex leading-edge curvature has been found to have a strongly stabilizing effect on boundary-layer modes but only a weakly stabilizing effect on acoustic modes. Furthermore, for certain parameter choices, the acoustic modes have been found to dominate the boundary-layer modes.

Key words: boundary-layer stability, compressible boundary layers

1. Introduction

Soon after the invention of the aircraft in the beginning of the twentieth century, it was realized that hydrodynamic instabilities of the Tollmien–Schlichting type trigger the laminar–turbulent transition process for unswept wings. With the advent of high-speed aircraft in the 1940s, the introduction of swept wings became necessary in order to overcome serious design problems emanating from compressibility effects, notably the shock stall phenomenon. The subsequent investigations on swept wings suggested that the presence of sweep does not affect the stability of the flow. However, in later flight tests on swept wing aircraft, Gray (1952) found that beyond a critical free stream velocity q_∞, the transition front moved towards the attachment line of the wing; this phenomenon could not be explained by existing two-dimensional arguments. He further observed that this critical free stream velocity depends on the sweep angle Λ as well as the leading-edge radius R of the wing.

The theoretical and experimental investigations that followed revealed a new type of instability, the crossflow instability (Gregory, Stuart & Walker 1955). The presence of sweep (and curvature) leads to a highly three-dimensional boundary-layer flow in the leading-edge region of a swept blunt body and, thus, fundamentally alters its inherent

† Email address for correspondence: christoph.mack@mytum.de

stability properties; the initially two-dimensional boundary layer along the attachment line gradually develops into a three-dimensional boundary-layer downstream of the attachment line (see, e.g., Bippes 1999, for a detailed description of the flow). The crossflow instability exhibits coherent co-rotating vortices whose axes are aligned with the streamlines of the external flow. The prevalence of crossflow vortices led to the hypothesis of a crossflow-vortex-induced transition.

New experiments revealed once more a lack of understanding of swept leading-edge flow, since they demonstrated that leading-edge transition – in particular, the phenomenon of leading-edge contamination caused by turbulent flow propagating along the leading edge (Gaster 1965; Pfenninger 1965) – cannot be explained by the crossflow instability mechanism alone. Based on wind-tunnel experiments on a swept wing model with a circular leading edge, Poll (1979) concluded that the flow is also susceptible to instabilities right at the attachment line. This general finding has become known as attachment-line instability. The above experimental results have fuelled a substantial effort to investigate the flow behaviour governed by the two identified mechanisms. These investigations, however, have been based on local flow models for either instability mechanism: (i) the swept Hiemenz flow model has been generally accepted as an approximation for the incompressible flow near the attachment line and has been studied, among others, by Hall, Malik & Poll (1984), Spalart (1988), Kazakov (1990), Joslin (1995, 1996) and Lin & Malik (1996, 1997, 1995); (ii) crossflow instabilities, which have been experimentally observed further downstream of the attachment line, have been studied using a local flow model based on a three-dimensional boundary layer. For an overview of the current state of the art, the reader is referred to, e.g., Saric, Reed & White (2003), Wassermann & Kloker (2003), Bonfigli & Kloker (2007) and references therein.

Up until about a decade ago, the two instability mechanisms have been investigated in isolation of each other. Despite hints from experimental efforts that a link between the two instability mechanisms may exist, the technical and numerical tools to investigate the two instabilities together were not available at that time. Attempts to establish a link between the two mechanisms have been undertaken by Spalart (1989) and Bertolotti (1999) using, respectively, direct numerical simulations (DNS) and parabolized stability equations (PSE) based on swept Hiemenz flow. A recent global stability analysis, focusing only on boundary-layer instabilities, of compressible flow about a swept parabolic body established a more definite connection between (local) attachment-line instabilities and (local) crossflow vortices (Mack, Schmid & Sesterhenn 2008).

Besides boundary-layer modes, the same flow model also contains additional instability mechanisms due to compressibility effects (see, e.g., Mack 1984). Furthermore, based on experience with semi-infinite flow geometries such as boundary layers, we expect the presence of continuous branches (Grosch & Salwen 1978; Balakumar & Malik 1992) in the global spectrum. The coupling of DNS with a standard iterative eigenvalue solver (Barkley & Henderson 1996; Mack *et al.* 2008; Bagheri *et al.* 2009) is insufficient to extract spectral information of such a complex flow configuration. Rather, a more advanced DNS-based global stability solver had to be developed (Mack & Schmid 2010*b*) that enables us to explore selected parts of the global spectrum and thus to gain a more complete picture of the (full) perturbation dynamics of the flow.

This paper is organized as follows. In §2 we present the three-dimensional flow model, including the governing parameters, the governing equations and details of the DNS code. In §3 we briefly introduce the concept of DNS-based global stability
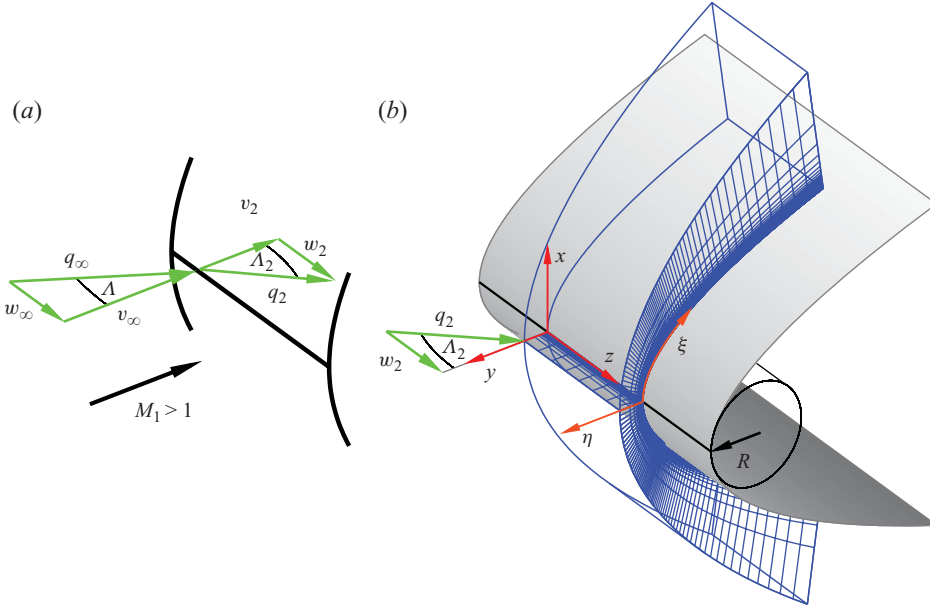
FIGURE 1. (*a*) Schematic of a detached bow shock (in black) and the relevant flow parameters upstream and downstream of the shock. (*b*) Sketch of the three-dimensional flow configuration.

analysis and its implementation. This is followed by the results in §4 where features of the global spectrum are discussed; concluding remarks are offered in §5.

2. Flow configuration, governing parameters and numerical method

The flow configuration, as displayed in figure 1(*b*), consists of a parabolic body (in grey) about which a three-dimensional body-fitted grid (in blue) is mapped. The local Cartesian coordinate system (in red) is given by the x-, y- and spanwise z-direction pointing along the attachment line (in black), and the local parabolic coordinate system (in orange) consists of the chordwise ξ- and the normal η-direction pointing along grid lines in the downstream direction and along grid lines normal to the wall, respectively. The surface of the parabolic body is given by

$$x(y) = \frac{1}{2R}y^2, \tag{2.1}$$

where R denotes its leading-edge radius. We consider flow situations where the oncoming flow is supersonic,

$$M_1 = M_\infty \cos \Lambda > 1, \tag{2.2}$$

where M_∞ and M_1 denote the free stream Mach number and its component normal to the shock, and Λ is the free stream angle (see figure 1*a*); thus, the computational domain is limited by a detached unsteady bow shock in the η-direction, and this shock, assumed to be an infinitely thin moving discontinuity, acts as the inflow boundary.

The supersonic flow state upstream of the detached bow shock, denoted by the subscript ∞, is given by the free stream Mach number M_∞ and the free stream angle Λ, and a total temperature $T_0 = 728$ K and total pressure $p_0 = 1.55 \times 10^6$ Pa are used as a reference state. From these quantities and the Rankine–Hugoniot relations, the

flow state downstream of the shock, denoted by the subscript 2, is obtained (see figure 1*a*). Consequently, the incoming flow impinges on the body with a velocity q_2 and a sweep angle Λ_2, yielding a sweep velocity w_2 and a normal velocity v_2. The latter quantities will be used in what follows to define the governing parameters.

2.1. *Governing parameters*

The flow configuration under investigation is characterized by two distinct length scales, the leading-edge radius R and a viscous length scale δ, which, respectively, describe the outer flow and the flow inside the boundary layer. We define this viscous length scale as

$$\delta = \left(\frac{v_r}{S}\right)^{1/2} \quad \text{with} \quad S = \left(\frac{\partial u}{\partial x}\right)_w = \frac{2v_2}{R}, \tag{2.3}$$

where S is the strain rate at the wall, at the attachment line, which follows from the chordwise derivative of the potential solution of flow around a circular cylinder with radius R, chosen as $R = 0.1$ m, evaluated at the stagnation point. The size of the length scale δ is depicted in figure 3(*c*) for a selected parameter choice.

We further define a sweep Reynolds number Re_s, a leading-edge Reynolds number Re_R, a sweep Mach number Ma_s and a wall temperature ratio θ_w as

$$Re_s = \frac{w_2 \delta}{v_r}, \quad Re_R = \frac{v_2 R}{v_r}, \quad Ma_s = \frac{w_2}{c_2}, \quad \theta_w = \frac{T_w}{T_r}, \tag{2.4}$$

where v_2 and w_2 are the wall-normal and sweep velocities downstream of the bow shock, c_2 stands for the speed of sound, and v_r denotes the kinematic viscosity evaluated at recovery temperature T_r and stagnation pressure p_s. In this paper, we consider an adiabatic wall, and thus the ratio of the temperature T_w at the wall and T_r is $\theta_w \approx 1$.

Alternatively, the sweep Reynolds number Re_s can be reformulated to display an explicit dependence on the leading-edge Reynolds number Re_R and the sweep angle Λ_2 as well as the leading-edge radius R:

$$Re_s = \left(\frac{Re_R}{2}\right)^{1/2} \tan \Lambda_2 = \frac{R}{2\delta} \tan \Lambda_2. \tag{2.5}$$

As we can see from (2.5), the sweep Reynolds number describes the influence of the sweep as well as the leading-edge curvature.

2.2. *Free stream dependence*

The governing parameters have been defined using the flow quantities downstream of the bow shock (see § 2.1), and these parameters depend on the free stream conditions in a nonlinear manner. As an example, using the definition of the sweep Mach number in (2.4), the thermodynamic relation for the speed of sound for a perfect gas, $c^2 = \gamma RT$, as well as the Rankine–Hugoniot relation for the temperature ratio T_2/T_1, the sweep Mach number can be computed via

$$Ma_s = \frac{\gamma + 1}{2} M_1^2 \tan \Lambda \left(\frac{1 - \gamma}{2} + \gamma M_1^2\right)^{-1/2} \left(1 + \frac{\gamma - 1}{2} M_1^2\right)^{-1/2}. \tag{2.6}$$

For the shock-free configuration, this relation reads

$$Ma_s = M_1 \tan \Lambda \left(1 + \frac{\gamma - 1}{2} M_1^2\right)^{-1/2}. \tag{2.7}$$
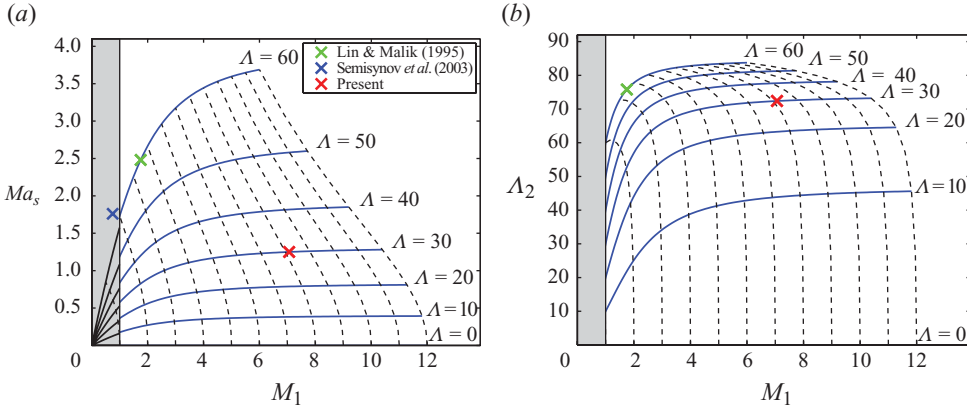
FIGURE 2. (*a*) Sweep Mach number Ma_s and (*b*) sweep angle Λ_2 as a function of the shock-normal Mach number $M_1 = M_\infty \cos \Lambda$ and the free stream angle Λ. The region in grey denotes the case where the oncoming flow is subsonic, i.e. $M_1 < 1$ (note that, in this case, $\Lambda_2 = \Lambda$), and the blue lines represent constant values of Λ while the dashed black lines depict constant values of M_∞. The red cross marks the free stream conditions of the present study, and the green and blue crosses represent the flow conditions which have been used in previous linear stability analyses.

Both (2.6) and (2.7) reveal a nonlinear dependence of Ma_s on the free stream conditions, and this dependence is given in figure 2. In figure 2(*a*), we show Ma_s as a function of M_1 and Λ, where the solid and the dashed lines represent constant values of Λ and M_∞, respectively. For instance, in this paper, we study a free stream Mach number $M_\infty = 8.15$ and a free stream angle $\Lambda = 30°$, yielding a shock-normal Mach number $M_1 = 7.06$, which results in a sweep Mach number $Ma_s = 1.25$. Since M_1 defines the shock-detachment distance and thus the size of the domain in the η-direction (see Mack & Schmid 2010*a*), this parameter choice results in a rather small domain in η. Furthermore, figure 2(*b*) demonstrates that since the sweep Reynolds number Re_s is a function of the sweep angle Λ_2 (see (2.5)), it also depends in a nonlinear manner on the free stream conditions.

2.3. *Numerical method*

We consider the motion of a compressible fluid modelled as a perfect gas with constant specific heat ratio $\gamma = 1.4$ and constant Prandtl number $Pr = 0.71$. The compressible Navier–Stokes equations, the equation of state, Fourier's law for the thermal conductivity and Sutherland's law (at ambient conditions) for the viscosity fully describe the flow. The equations are formulated based on pressure p, Cartesian velocities (u, v, w) and entropy s, and are solved on a time-dependent, curvilinear and non-uniformly distributed grid, with a clustering of the grid points towards the wall as well as in the leading-edge region, as shown in figure 1(*b*).

For the DNS in this study, the computational domain is limited by a detached unsteady bow shock, assumed to be an infinitely thin moving discontinuity, in the wall-normal direction. This discontinuity is incorporated through a shock-fitting technique (Moretti 1987) and provides the inflow conditions via the Rankine–Hugoniot relations. Along the surface of the body, no-slip boundary conditions and adiabatic wall conditions are applied. At the chordwise edges of the computational domain, non-reflecting outflow boundary conditions are imposed and, under the assumption of

infinite span, periodic boundary conditions are used in the z-direction. For details on the implementation of the numerical procedure such as the spatial and the temporal discretization, we refer the reader to Mack & Schmid (2010*a*). The homogeneity in the spanwise z-direction allows us to Fourier transform this direction, and the remaining inhomogeneous η- and ξ-coordinate directions are discretized by compact finite-difference schemes using 128×255 grid points, respectively.

3. Global stability analysis

Information about the disturbance behaviour for complex geometries and/or complex flow physics relies on the formulation of a global stability problem when limiting assumptions such as locally parallel flow, multiple homogeneous coordinate directions or a low-Mach-number approximation are undesirable or impossible. For a comprehensive understanding of the perturbation dynamics for our flow configuration (see figure 1), neither of the above-mentioned limiting assumptions should be made; rather, a global formulation of the stability problem has to be attempted. For this reason, we assume a three-dimensional perturbation field $\phi' = (p', u', v', w', s')^{\mathrm{T}}$ superimposed on a (steady) base flow ϕ_0 according to

$$\phi(x, y, z, t) = \phi_0(x, y, z) + \epsilon \phi'(x, y, z, t), \quad \epsilon \ll 1. \tag{3.1}$$

We proceed by computing a base flow as a steady solution of the nonlinear compressible Navier–Stokes equations, and a subsequent linearization about this base flow yields the linearized Navier–Stokes equations for the perturbations ϕ' which can formally be written as

$$\frac{\partial \phi'}{\partial t} = \mathscr{J}(\phi_0)\phi', \tag{3.2}$$

with $\mathscr{J}(\phi_0)$ denoting the linear stability operator (the Jacobian).

3.1. *Base flow*

The assumption of infinite span permits us to eliminate the z-dependence, but not the w-component, from the base flow $\phi_0(x, y, z)$ and to reduce the computations to a problem with only two independent variables x and y. From the solution of a long-time integration, the full three-dimensional base flow can be recovered. This procedure is possible since the flow is stable with respect to two-dimensional perturbations, thus allowing a simple time-integration towards a steady state. As a consequence, more sophisticated techniques such as Newton-type methods (Jacobian-free), Newton–Krylov techniques (Knoll & Keyes 2004) or selective frequency damping (Åkervik *et al.* 2006) can be avoided.

An initial two-dimensional flow field has thus been integrated in time until a steady state has been reached to within a sufficiently high accuracy. For a detailed discussion of the required quality of this steady base flow and the distinction between base and mean flow for global stability problems, the reader is referred to Theofilis (2003) and Sipp & Lebedev (2007). The converged three-dimensional base flow is visualized, in terms of streamlines and pressure field, in figure 3(*a*). In addition, the local and nearly two-dimensional flow field in the vicinity of the leading edge is depicted in figure 3(*c*) shown by the normal and streamwise velocities. The three-dimensional base velocity profile further downstream from the attachment line is illustrated in figure 3(*b*). It represents a typical profile of a three-dimensional boundary layer consisting of twisted velocity vectors inside the boundary layer which eventually align with the curved streamlines of the inviscid outer flow.
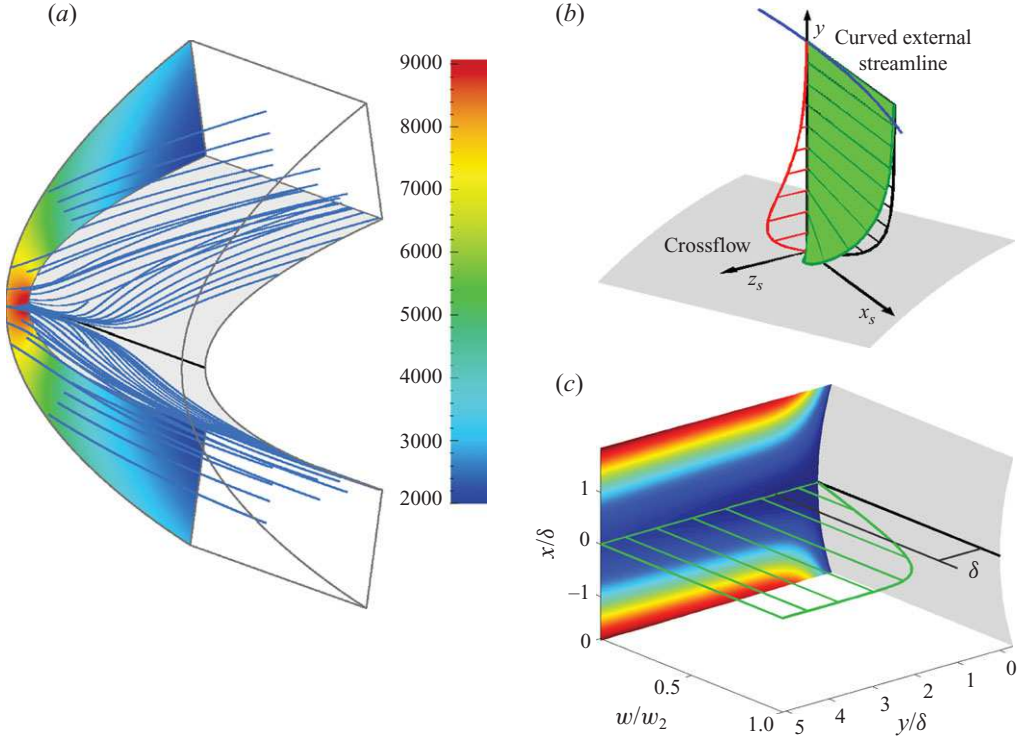
FIGURE 3. (*a*) Streamlines (in blue) and pressure field (in Pa) of the computed steady base flow for $Re_s = 800$, $Re_R = 129\,136$, $Ma_s = 1.25$ and $\theta_w \approx 1$; attachment line in black. (*b*) Schematic of the three-dimensional boundary layer at a selected position downstream of the attachment line (adapted from Bippes 1999). (*c*) Normalized w-velocity profile, stretched by a factor of 100 in η, along the attachment line; the normal velocity v is shown at the back as the coloured shading and $\delta = 1.968 \times 10^{-4}$ m for the present parameter choice.

3.2. *DNS-based global stability solver*

This three-dimensional base flow forms the starting point for our DNS-based global stability analysis. The details of this stability solver are given in Mack & Schmid (2010*b*), but for the sake of completeness, we briefly outline and discuss its main features.

Assuming a disturbance field (see (3.1)) of a travelling-wave form,

$$\phi'(x, y, z, t) = \widetilde{\phi}(x, y)\, e^{i(\beta z - \omega t)}, \tag{3.3}$$

where $\widetilde{\phi}(x, y)$ denotes the complex amplitude and β the real spanwise wavenumber of the perturbation; the temporal long-term evolution of the disturbance is characterized by ω whose real part ω_r describes the frequency and whose imaginary part ω_i represents the growth rate. Upon substitution of expression (3.3) into the linearized compressible Navier–Stokes equations (3.2) and subsequent discretization in the remaining coordinate directions, we can formally write the global discrete stability problem as

$$\omega\, \widetilde{\boldsymbol{\phi}} = \boldsymbol{J}(\boldsymbol{\phi}_0)\, \widetilde{\boldsymbol{\phi}}. \tag{3.4}$$

Herein, the matrix $J(\phi_0)$ represents the linear stability matrix (the Jacobian). The direct solution of the resulting discrete $n \times n$ eigenvalue problem, where $n = 5n_\xi n_\eta$ (with n_ξ and n_η as the number of grid points in the chordwise and normal direction) denotes the size of $J(\phi_0)$ and typically is of the order $O(10^6 – 10^7)$, is prohibitively expensive. For this reason, iterative solution techniques have to be employed to extract pertinent stability information.

The algorithm to accomplish this task is the implicitly restarted Arnoldi method (IRAM), a Krylov subspace technique presented by Sorensen (1992), which is publicly available and described in Lehoucq, Sorensen & Yang (1998). This class of techniques requires only the action of the Jacobian matrix $J(\phi_0)$ onto a given velocity field ϕ'. These matrix-vector products can be obtained readily from DNS via

$$J(\phi_0)\phi' \approx \frac{F(\phi_0 + \epsilon\phi') - F(\phi_0)}{\epsilon} = \left.\frac{\partial F(\phi)}{\partial \phi}\right|_{\phi=\phi_0} \phi' + O(\epsilon), \qquad (3.5)$$

where ϵ is a user-specified parameter, chosen as $\|\epsilon\phi'\|/\|\phi_0\| = \epsilon_0 = 10^{-8}$, and F represents the right-hand side of the nonlinear Navier–Stokes equations. This approximation avoids the explicit formulation and storage of the Jacobian matrix and thus allows a Jacobian-free framework where our DNS code provides the input for the iterative stability solver. For a discussion on the choice of the parameter ϵ_0, see Mack & Schmid (2010*b*). In the same reference, it was further demonstrated that a spectral transformation such as the Cayley transformation is necessary to accelerate and control the convergence of the iterative eigensolver by judiciously deforming the complex plane. In addition, this same spectral transformation adds to the robustness of the solver and allows the Krylov subspace method to converge towards specific parts of the complex global spectrum. The Cayley transformation consists of a two-parameter conformal mapping defined as

$$T_C(\sigma, \mu) \equiv (J(\phi_0) - \sigma I)^{-1}(J(\phi_0) - \mu I), \quad \omega = \frac{\sigma\lambda - \mu}{\lambda - 1}, \qquad (3.6)$$

where σ and μ denote the mapping parameters, and I is the mass matrix, in our case the identity matrix. The computed region of the full global spectrum depends on the choice of these parameters, most notably on the choice of the shift parameter σ. The desired eigenvalues ω of $J(\phi_0)$ can be recovered straightforwardly from the eigenvalues λ of the transformed problem. The advantages of this transformation (see (3.6)), however, come at the expense of solving a linear system which, in keeping with the overall iterative nature of our global stability method, has to be done iteratively by a Krylov subspace technique, in our case the BiCGStab method (van der Vorst 1992) with an ILU-type (incomplete LU decomposition) pre-conditioner (Saad 2003). Details can be found in Mack & Schmid (2010*b*).

4. Results

The iterative algorithm outlined in §3.2 is applied to simulations of compressible flow around a swept parabolic body, as depicted in figure 1. As the Krylov subspace is augmented by subsequent calls to the DNS code, the ILU-pre-conditioned Cayley-transformed Arnoldi method provides an approximate spectrum that consequently increases not only in complexity but also in accuracy.

4.1. *Global spectrum*

The computed global spectrum (see figure 4) reflects the richness of physical processes present in the flow configuration under investigation. It consists of (mostly unstable)
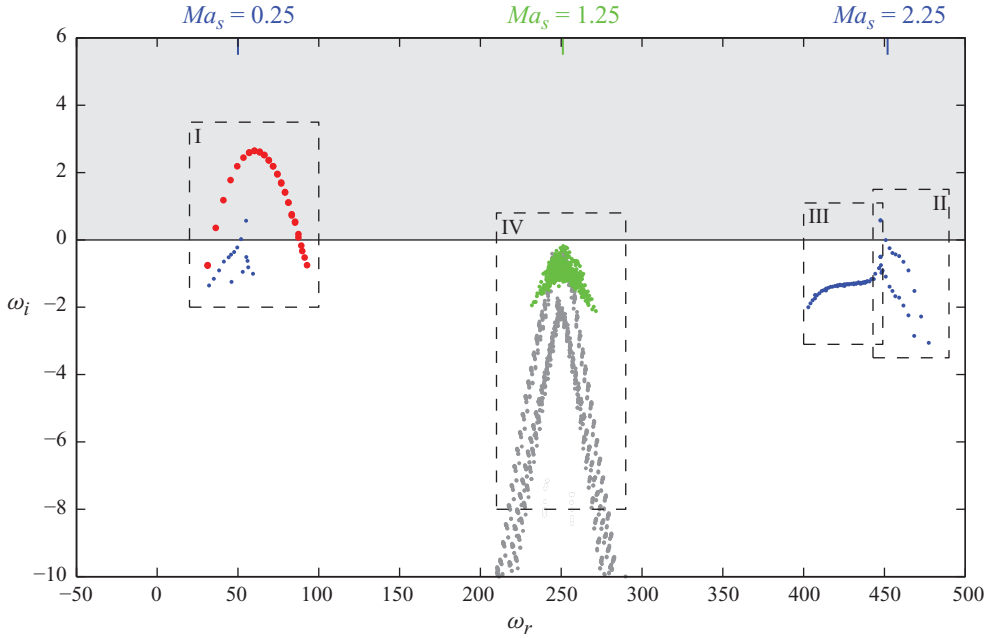
FIGURE 4. Global spectrum showing the frequency ω_r and the corresponding growth rate ω_i of the iteratively computed modal structures ($Re_s = 800$, $Re_R = 129\,136$, $Ma_s = 1.25$, $\theta_w \approx 1$ and $\beta = 0.314$); the eigenvalues ω have been non-dimensionalized using the strain rate S. Each region shows the least-stable eigenvalues belonging to boundary-layer modes (region I), acoustic modes (regions I, II and III), and wavepacket modes (region IV); unstable-half-plane in grey. The most unstable modes in region I were presented in Mack *et al.* (2008).

discrete shear modes (region I, in red) that express the flow characteristics inside the boundary layer, of acoustic modes that describe the presence of (stable and unstable) sound waves (regions I–III, in blue) and of (stable) wavepacket modes (region IV, in green) that represent the dynamics of general perturbations outside the boundary layer; the latter type of modes is complemented by the partial spectrum (region IV, in grey) obtained by directly solving for the eigenvalues of the Jacobian matrix for an embedded and significantly smaller sub-domain located near the attachment line. For the current parameter choice – i.e. a sweep Reynolds number of $Re_s = 800$, a leading-edge Reynolds number of $Re_R = 129\,136$, a sweep Mach number of $Ma_s = 1.25$, an adiabatic wall ($\theta_w \approx 1$) and a disturbance wavenumber $\beta = 0.314 = 2\pi/L_z$ (with L_z the fundamental length scale of the perturbations, non-dimensionalized by the viscous length scale δ, in the spanwise z-direction) – the discrete boundary-layer branch (in red) features the most unstable global modes.

The global spectrum (see figure 4) also shows that the physical processes described by different types of global modes exhibit a distinct but characteristic frequency ω_r. The boundary-layer modes (in red), for instance, prevail inside the boundary layer, and the displayed modes travel with a phase speed of approximately 12 %–37 % of the (mean) velocity, $w_{mean} \approx w_2$, in the spanwise z-direction ($\omega_{r,mean} = w_2\beta/(S\delta)$ with $w_2 = 583.1\,\text{m s}^{-1}$, $\delta = 1.968 \times 10^{-4}\,\text{m}$ and $S = 3704\,\text{s}^{-1}$). The acoustic modes (in blue), on the other hand, travel downstream and upstream in z with $w_2 \pm c_2$, where c_2 stands for the speed of sound in the free stream. This speed of $w_2 \pm c_2$ corresponds to Mach numbers $Ma_s = (w_2 \pm c_2)/c_2$ of 2.25 and 0.25 (see figure 4). The wavepacket modes (in
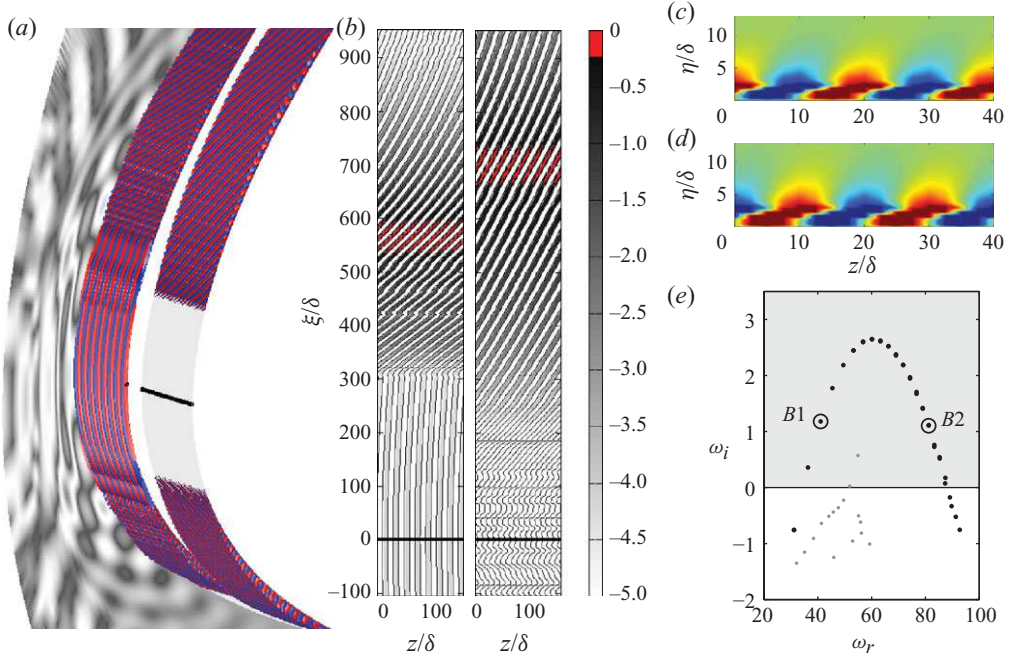
FIGURE 5. (*a*) Two representative global modes from the boundary-layer branch visualized by iso-surfaces (positive values in red, negative values in blue) of the normal velocity $v(x, y, z) = \text{Re}\{\tilde{v}(x, y)(\cos \beta z + \mathrm{i} \sin \beta z)\}$; eight periods in z are shown. The left and right modes, respectively, correspond to the two eigenvalues $B1$ and $B2$ depicted by circles in (*e*); contours of the associated pressure field are shown in the background; attachment line in black. (*b*) Top view of v in the ξ–z plane at approximately half the boundary-layer thickness; a log scale is used to visualize the positive values of v. (*c*, *d*) Chordwise cross-cuts of v at $\xi/\delta \approx 400$ and $\xi/\delta \approx 580$. (*e*) Region I of the global spectrum shown in figure 4.

green) move with approximately the (mean) velocity w_2 since they mainly capture the dynamics of perturbations in the free stream. The frequencies of the respective modes and an argument about their local propagation speed thus allows a first classification of the eigenvalues as well as an estimate of the localization of the corresponding global modes within the computational domain.

4.1.1. *Boundary-layer modes*

Concentrating on boundary-layer modes (in red, see region I in figure 4), the employed global stability solver identified an eigenvalue branch of typical parabolic shape. This branch consists of stable and unstable discrete modes whose frequency ω_r ranges from 31.1 to 92.8 (see figure 5*e*); the maximum growth rate, $\omega_i = 2.64$, is achieved for $\omega_r = 60.1$. Owing to the inherent symmetry properties of the flow, the eigenvalues appear double at closer inspection, and the associated modes exhibit characteristic symmetry properties with respect to the attachment line. As the symmetry of the base flow is broken, such as by introducing an angle of attack, the coalescence of two respective eigenvalues from the boundary-layer branch is expected to vanish, giving rise to two slightly displaced parabolic arcs.

Two representative global modes, labelled $B1$, $B2$, and indicated by black circles in figure 5(*e*), are visualized by iso-surfaces of the normal velocity v in figure 5(*a*). The slower moving mode $B1$ displays typical features of both attachment-line instabilities

and crossflow vortices, as previously reported by Mack *et al.* (2008). The faster moving mode $B2$ shows a substantially stronger component of the crossflow instability, and its maximum amplitude is located further downstream from the attachment line. This property is more evident in figure 5(b), where we present a body-fitted cross-cut at a distance of half the boundary-layer thickness from the wall. The same figure also demonstrates the two-dimensional character of the global modes near the attachment line (see mode $B1$). Further downstream, both modes display the typical curved shape of crossflow instabilities. With the spanwise wavenumber $\beta = 2\pi/L_z$ held constant for both modes, the clearly visible difference in the spatial orientation of the crossflow vortices is a consequence of a corresponding difference in the equivalent 'local chordwise wavenumber'. This same 'local chordwise wavenumber' parameterizes the parabolic eigenvalue branch of the associated global boundary-layer modes in figure 5(e). An equivalent parabolic shape would be obtained in *local* stability analyses as the least-stable eigenvalue is traced as a function of the chordwise wavenumber. Figure 5(c, d) depicts two chordwise cross-cuts of the normal velocity v at two selected positions, (c) at $\xi/\delta \approx 400$ and (d) at the location of the maximum amplitude of $B1$.

The compressible nature of the flow is expressed in the existence of an associated weak pressure field, which reflects the acoustic footprint of a global shear mode. This phenomenon is visualized in the ξ–η plane by contours of the pressure for the boundary-layer mode $B1$ (see figure 5a).

Due to the global nature of the analysis, the modes from the boundary-layer branch display a complex spatiotemporal behaviour. The temporal behaviour is captured by the eigenvalues while the associated spatial characteristics are represented by the eigenfunctions. In analogy to local analyses, the exponential growth of individual modes (as observed for our parameter settings) has to be examined and evaluated in the light of the limitations of a linear model, the necessity of superposing individual modes to describe short-time behaviour as well as the saturating and modifying effects of nonlinearities. It is also important to keep in mind that, even though the global modes displayed in figure 5 show features familiar from local analyses, the extracted global modes are best interpreted as compound quantities that do not necessarily have to strictly adhere to the local characteristics of accustomed attachment-line or crossflow modes.

4.1.2. *Acoustic modes (type A)*

Due to the presence of compressibility, the global spectrum also features distinct sets of slow- and fast-moving acoustic global modes (see blue dots in regions I and II in figure 4) which describe the presence of sound waves. These modes travel with approximately $w_2 \pm c_2$ in the spanwise z-direction, as already discussed in §4.1. In figure 6(a), we display region II of the global spectrum (see figure 4) which contains the fast-moving set of acoustic modes. It is found that these modes can be divided into symmetric S modes – the spatial distribution of all disturbance quantities except for the chordwise velocity u is symmetric with respect to the attachment line – and antisymmetric A modes. We again note that this symmetry property will disappear in the case of a non-symmetric base flow profile (e.g. due to a non-zero angle of attack). Each S mode is found to pair with an A mode at the same frequency ω_r, e.g. $\omega_{r,S2} = \omega_{r,A2}$ (see dashed line in figure 6a). Moreover, either type of modes describes a distinct branch in the eigenvalue spectrum, indicated by the grey line in figure 6(a), where the modes on the A branch are always more stable than the modes on the S branch.
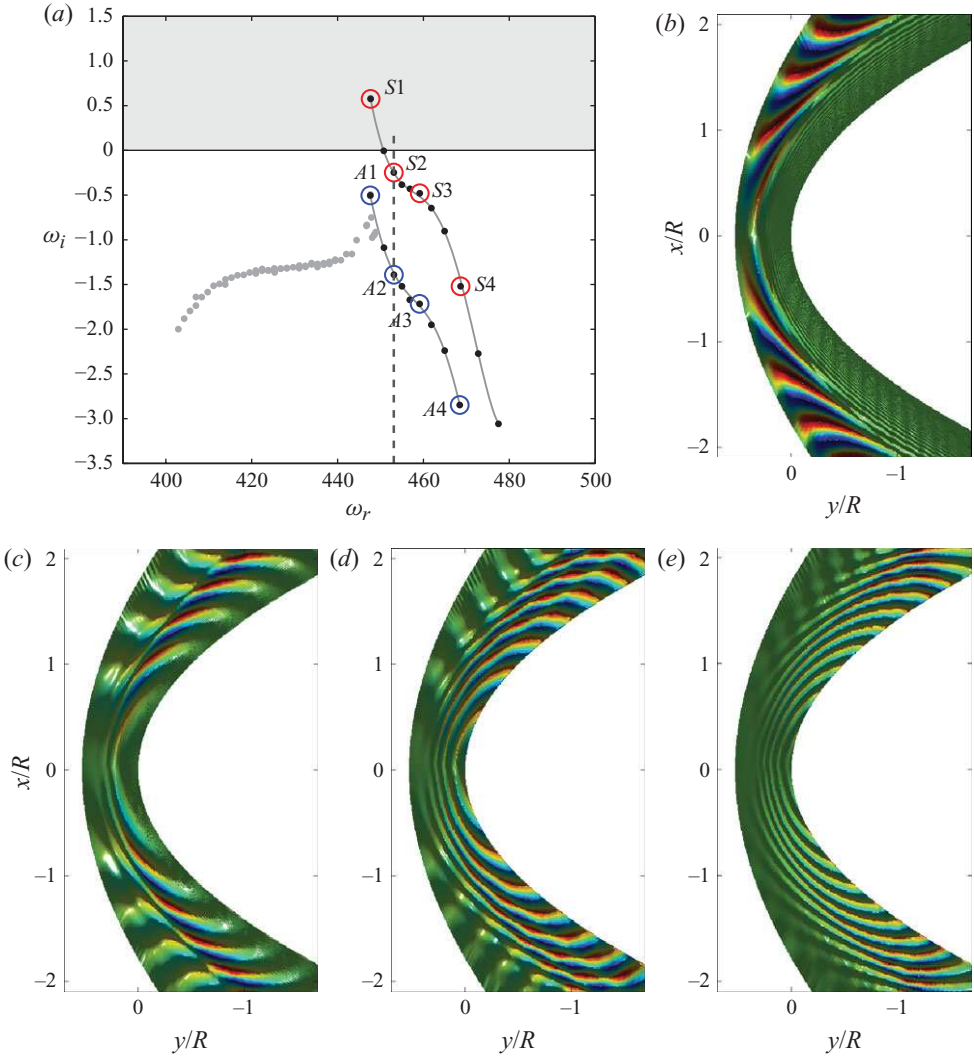
FIGURE 6. (*a*) Computed region of the global spectrum containing the fast-moving set of acoustic modes (see regions II and III in figure 4). (*b*–*e*) Spatial structure of a sample of associated global acoustic modes belonging to the eigenvalues *S*1, *S*2, *S*3 and *S*4 from the *S*-branch depicted by red circles in (*a*). The modes are visualized by the chordwise velocity $u(x, y, z)$ in the x–y plane. The green hue corresponds to vanishing amplitudes (larger amplitudes in red); $R = 0.1 = 508\delta$.

The spatial structure of a representative sample of acoustic modes from the *S* branch is presented in figure 6(*b*–*e*); the corresponding eigenvalues of these modes are circled in red in figure 6(*a*) and denoted by *S*1–*S*4, respectively. All modes are visualized by the amplitude distribution of the chordwise velocity u in the x–y plane. The unstable (*S*1) and the marginally stable modes (*S*2) reveal a dominant spatial structure downstream of the detached bow shock, and this structure decays towards the surface of the body; the bow shock acts as a flexible 'wall', which prevents sound waves from travelling upstream of the shock. More stable modes (*S*3 and *S*4) are more pronounced in the half of the physical domain which is adjacent to the body,
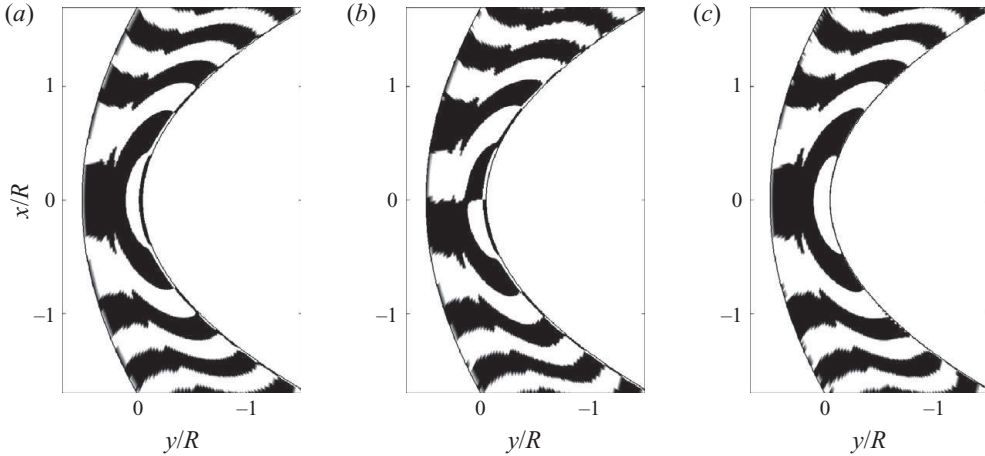
FIGURE 7. Sign of the pressure distribution, sign(p), of selected global acoustic modes in the x–y plane: (a) S mode ($S2$) and (b) A mode ($A2$) from the fast-moving set of acoustic modes (see figure $6a$); (c) mode corresponding to $S2$, from the slow-moving set of acoustic modes denoted by $\bar{S}2$ (see blue dots in region I in figure 4).

and they exhibit smaller spatial structures as they are increasingly tilted and damped; the smaller spatial structures are the result of this obliqueness of the waves.

The smaller the spatial structures, the larger is the chordwise 'wavenumber' α and thus the propagation angle of the acoustic waves. The unstable mode $S1$ exhibits a small value of α and thus displays an approximately two-dimensional wave travelling in the spanwise z-direction. This mode further shows no strong interaction with the shock; rather, the bow shock reacts to the structure of the mode by adjusting its spatial shape. However, for larger values of α, the oblique travelling acoustic waves strongly interact with the bow shock resulting in a small energy loss ($S2$). Finally, for even larger chordwise 'wavenumbers', α structures close to the parabolic body prevail ($S3$ and $S4$).

In figure 7, we present a comparison of three acoustic global modes belonging to the S and the A branch of the fast-moving set of acoustic modes (see region II in figure 4) as well as an acoustic mode from the corresponding slow-moving symmetric branch (marked by blue dots in region I in figure 4). As an example, we concentrate on mode $S2$ and its associated mode $A2$ (see dashed line in figure $6a$). From the slow-moving set of acoustic modes we choose the image mode (denoted by $\bar{S}2$) to $S2$, i.e. the mode with the identical decay rate ω_i as $S2$ but with a frequency of approximately $\omega_r \approx w_2 - c_2$. Regarding the spatial shape of these three modes, it is found that the sign of the pressure distribution, sign(p), is nearly identical (see figure 7). Besides the above-mentioned chordwise symmetric/antisymmetric structure of these modes, the two fast-moving modes exhibit a characteristic wall layer that decreases as we proceed downstream from the attachment line (figure $7a$, b); this feature is absent for the slow-moving mode $\bar{S}2$ (figure $7c$).

4.1.3. *Acoustic modes (type B)*

In addition to the acoustic modes presented in §4.1.2, another type of global acoustic modes exists. The dominant part of these modes lies in the free stream, and they display a characteristic structure in a local region between the detached bow shock and the attachment line (see figure 8). Starting with the global mode in
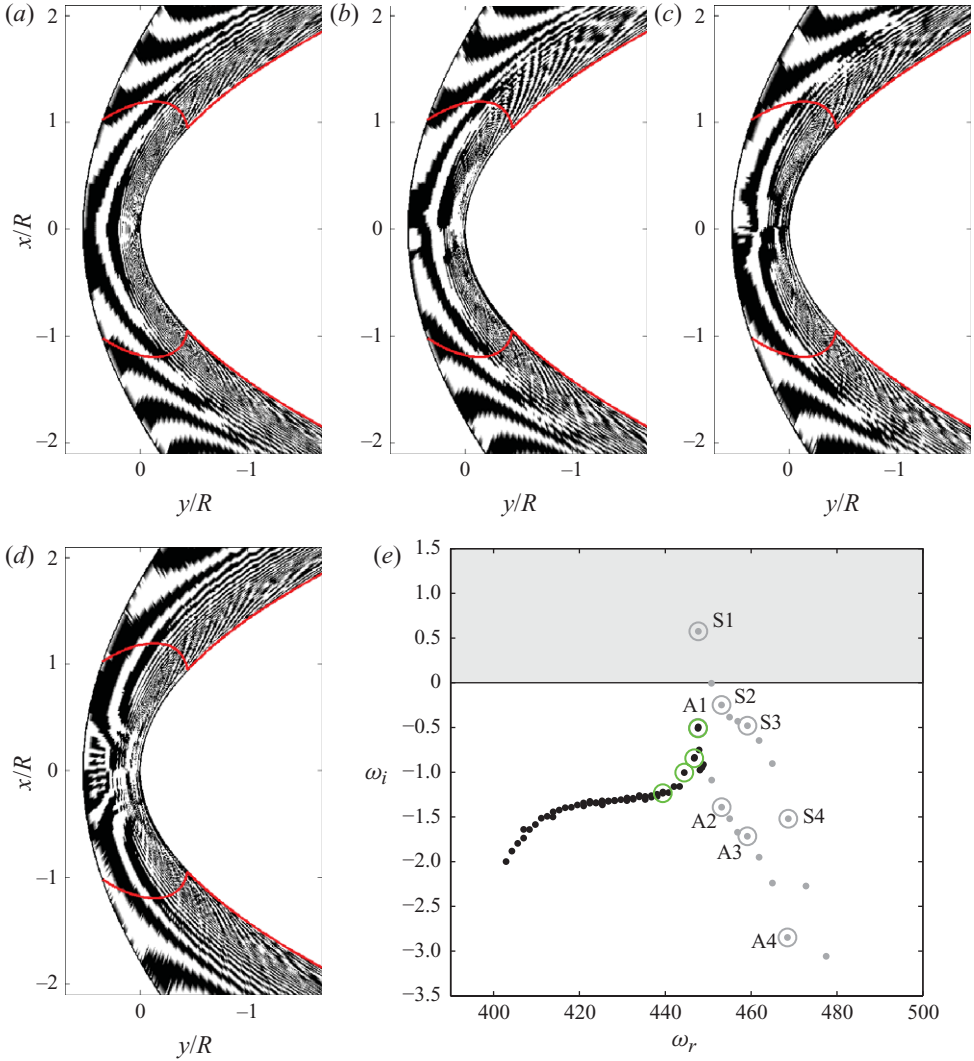
FIGURE 8. (*a*–*d*) Sample of a further type of global acoustic modes visualized by the sign of the chordwise velocity, sign(u), in the x–y plane; sonic line, i.e. $Ma = (u^2 + v^2)^{1/2}/c = 1$, in red. (*e*) The black dots display the corresponding eigenvalues in the global spectrum (see region III in figure 4); the eigenvalues circled in green belong to the global modes (*a*–*d*).

figure 8(*a*), which represents the first mode $A1$ of the A branch shown in §4.1.2, we again observe a symmetric spatial distribution for the chordwise velocity component u in the free stream (visualized by the sign of u). As we proceed along the eigenvalue branch marked in black in figure 8(*e*), an interesting behaviour emerges. It appears that a localized region between the bow shock and the attachment line decouples itself – in terms of distinct spatial scales – from the regions downstream from the attachment line. This decoupling is already visible, even though barely, in figure 8(*a*) directly behind the bow shock at $x = 0$. Progressing farther along the eigenvalue branch, this feature becomes more pronounced as the localized region further extends in a semi-circular fashion from its point of origin towards the body, and as the

structure within shows increasingly finer scales (see figure 8*b–d*). It appears that the symmetry properties of the structures inside and outside the localized region are uninfluenced by each other. The range of scales, on the other hand, indicates a link between the two regions: generally speaking, the smaller the scales inside the localized region, the coarser the structures on the outside (see figure 8*d*).

This type of modes is believed to account for the interaction of a moving flexible shock and a rigid curved surface, and these modes are reminiscent of localized standing waves. The increasingly finer spatial scales of the higher order modes are linked to higher damping rates. The localized spatial shape of the modes is also influenced by the different reflective behaviour (impedance) of acoustic waves by the curved solid surface (perfect reflection) and the curved flexible shock (imperfect reflection).

Acoustic modes of either type described above capture the propagation of sound due to compressibility of the fluid. Their source and the characteristics of their propagation are given by the perturbations in the boundary layer as well as the properties of the moving bow shock. The parabolic body with its boundary layer and the detached shock imperfectly reflect acoustic waves and thus act as a curved waveguide, which, in turn, imprints a specific stability behaviour onto the acoustic part of the spectrum. It is thereby not surprising that the acoustic modes show a considerable degree of complexity – making their direct interpretation difficult. The dynamics of the acoustic components, their role in the overall flow behaviour and (in the case of unstable acoustic modes) their saturation due to nonlinear interactions with other flow structures are best studied by DNS, starting with particular acoustic modal perturbations. A detailed investigation is beyond the scope of this paper and is left to a future effort.

4.1.4. *Wavepacket modes*

Returning to the global spectrum in figure 4, a distinct set of eigenvalues centred on the mean spanwise velocity is clearly visible. Region IV is again plotted in figure 9(*a*), and it shows a dense clustering of damped eigenvalues confined to a triangular-shaped region. The exact location of individual eigenvalues within this region is highly sensitive to numerical details. For this reason, it can be assumed, and will be later argued, that this part of the spectrum consists of an area which is progressively filled by the discrete eigenvalues as the numerical parameters (resolution, starting vector, Cayley parameters, convergence tolerances, etc.) but the physical parameters are not varied.

The location and distribution of the eigenvalues in region IV suggest a link to the continuous spectrum, familiar from boundary layers (Grosch & Salwen 1978; Balakumar & Malik 1992) and other semi-infinite and bi-infinite viscous shear flows. In the boundary-layer case, the continuous spectrum can be determined by a constant-coefficient Orr–Sommerfeld equation for the free stream. Its solutions are given by bounded exponential and trigonometric functions; the location of the spectrum is defined by a line parameterized by an equivalent wall-normal wavenumber.

In contrast, our governing equations evaluated in the free stream still retain a dependence on the wall-normal coordinate via the non-uniform base velocity. As a consequence, the solutions in the free stream are no longer wave trains (as, for instance, in the boundary layer) but rather localized wavepackets. As an example, three representative modes ($W1$, $W2$ and $W3$) from region IV are displayed in figure 9(*b*), which shows the spatial distribution of u in the normal direction in the form of a wavepacket; this property is even more visible in figure 10, where we present
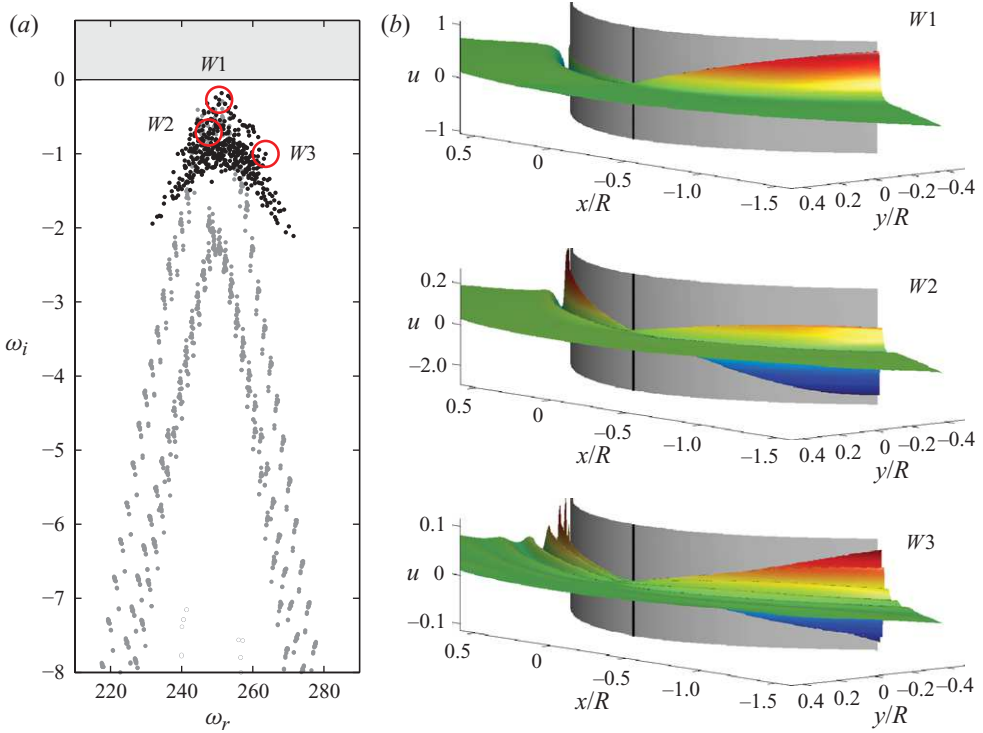
FIGURE 9. (*a*) Computed region of the global spectrum containing the eigenvalues belonging to wavepacket modes (see region IV in figure 4). (*b*) Three representative wavepacket modes (*W*1, *W*2 and *W*3) are visualized by the (normalized) chordwise velocity u; attachment line in black.
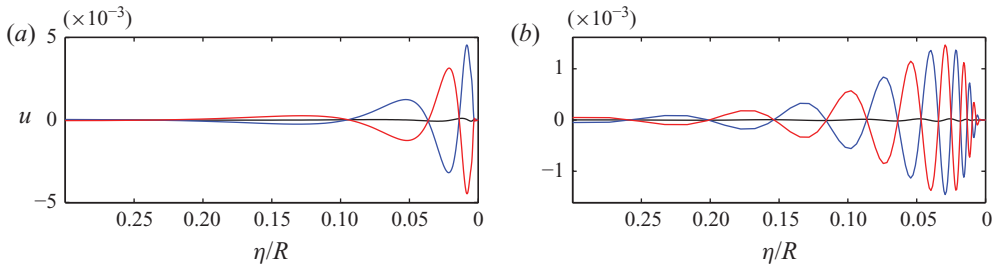

FIGURE 10. Amplitude distribution of two wavepacket modes shown in figure 9: (*a*) *W*2 and (*b*) *W*3. The modes are visualized using cross-cut profiles at the attachment line (in black) and at selected positions near the attachment line.

cross-cut profiles of *W*2 and *W*3 in the normal direction near the attachment line. These cross-cuts also demonstrate, even though barely visible, that the wavepacket modes extend into the boundary layer and thus establish a connection between boundary-layer and exterior perturbation dynamics. They are thus certain to play a critical role in the receptivity of boundary-layer instabilities to the external disturbance environment.

A consequence of the wavepacket shape is its parameterization by *two* variables, a wall-normal local wavenumber and the location of the wavepacket peak (Trefethen 2005; Obrist & Schmid 2010). For this reason, the associated continuous spectrum is area-filling as the continuous spectrum for the boundary layer was line-filling due to only *one* variable, the wall-normal local wavenumber.

Despite the marked sensitivity of the eigenvalues corresponding to wavepacket modes, these modes carry physical significance as they describe a link between free stream processes and boundary-layer perturbations. In this respect, wavepacket modes are instrumental in describing transition processes in the boundary layer triggered by external disturbances via a receptivity mechanism; particularly in the absence of acoustic effects they establish the only connection between the free stream and boundary-layer dynamics. The role of continuous (predominantly free stream) and discrete (predominantly boundary layer) modes in the transition process triggered by external disturbances has been established in the work of Zaki & Durbin (2005) and Liu, Zaki & Durbin (2008); analogous mechanisms are expected to be at play in the receptivity process of compressible flow about a swept parabolic body.

4.2. *Parameter studies*

Compressible flow around a swept parabolic body is governed by a large number of parameters describing various flow quantities, fluid properties and geometric characteristics of the flow configuration. For a particular choice of parameters, i.e. $Re_s = 800$, $Re_R = 129\,136$, $Ma_s = 1.25$, $\theta_w \approx 1$ and $\beta = 0.314$, the global spectrum (see figure 4) revealed that the only temporal instabilities arise from boundary-layer and/or acoustic modes. To gain further insight into the global stability properties of both types of instabilities, we present a parametric study of their stability behaviour by varying the spanwise disturbance wavenumber, $\beta = 2\pi/L_z$, and the leading-edge Reynolds number, Re_R. In particular, we focus on the stability of the global modes in regions I and II in figure 4.

The first parametric study allows us to investigate the linear stability of a computed base flow with respect to spanwise-propagating perturbations with a fundamental length scale L_z. The second parametric study assesses the influence of the leading-edge Reynolds number Re_R, via the leading-edge radius R, on the stability of the flow. This influence is particularly important for the global stability of the boundary-layer modes. Such a study requires, for each value of Re_R, the computation of a steady base flow, even though the free stream conditions remain fixed. For all other types of parameter studies, for example, the influence of the sweep Reynolds number $Re_s = Re_s(M_1, \Lambda)$ or the sweep Mach number $Ma_s = Ma_s(M_1, \Lambda)$, the nonlinear dependence between the governing parameters (see §2.2) requires a substantial effort for a systematic exploration of the four-dimensional parameter space.

4.2.1. *Influence of the spanwise disturbance wavenumber β*

The influence of the spanwise disturbance wavenumber on the boundary-layer modes was already discussed in Mack *et al.* (2008) for $0.090 \leqslant \beta \leqslant 0.314$, where they found a maximum modal growth for $\beta = 0.213$. For a more comprehensive parameter study, the application of the Cayley-transformed Arnoldi method, as employed in this paper, was found to be mandatory for accessing selected parts of the global spectrum and to investigate a larger range of spanwise wavenumbers β. The computed temporal spectra of the (most unstable) boundary-layer modes are shown in figure 11(*a*) for $0.071 \leqslant \beta \leqslant 0.349$. For a given value of β, the frequency ω_r and its corresponding growth rate ω_i reveal an unstable discrete branch, as discussed in §4.1.1. Each branch
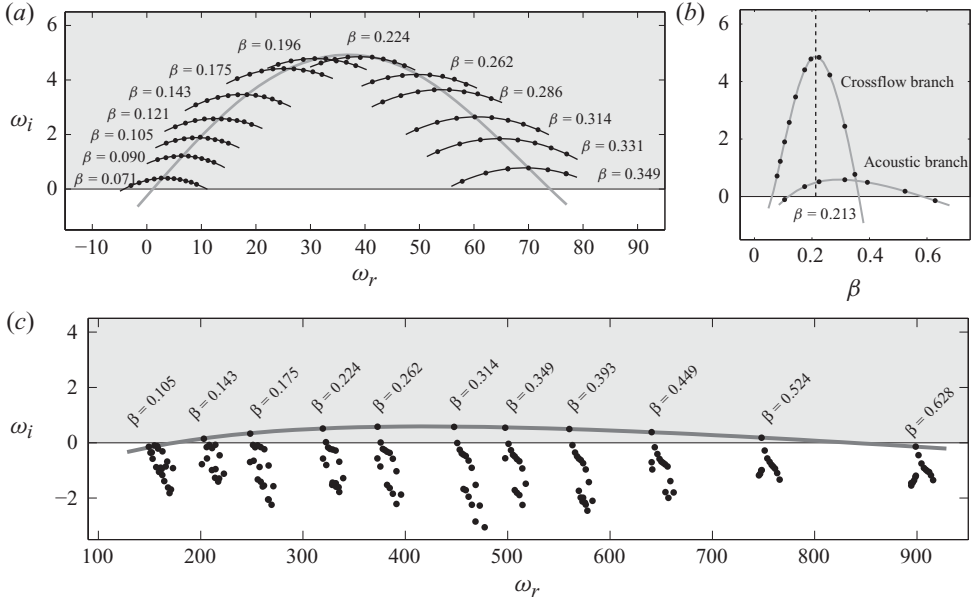
FIGURE 11. Influence of the spanwise disturbance wavenumber β on the stability of the flow: (*a*) temporal spectra of the least-stable boundary-layer modes for selected values of β; unstable half-plane in grey. The solid line in dark grey describes the evolution of the maximum temporal growth rate $\omega_{i,max}$, and the evolution of $\omega_{i,max}$, denoted by crossflow branch, as a function of β is shown in (*b*); (*c*) temporal spectra and evolution of the maximum temporal growth rate $\omega_{i,max}$ of the least-stable acoustic modes; the corresponding acoustic branch is displayed in (*b*).

displays a maximum value of the growth rate ω_i, and this value appears to grow steadily up to a specific wavenumber β before decaying again (see crossflow branch in figure 11*b*). Figure 11(*b*) also indicates that the boundary-layer modes are unstable for $0.061 \leqslant \beta \leqslant 0.363$.

By adjusting the parameters in the Cayley transformation (3.6), we are also able to focus on the computation of fast-moving acoustic modes (see region II in figure 4). In figure 11(*c*), we present the influence of β on the stability of these modes. We observe clusters of discrete acoustic eigenvalues where the least-stable mode belongs to the S branch. This mode is similar to the most unstable boundary-layer mode, unstable for a specific range of spanwise wavenumbers, $0.118 \leqslant \beta \leqslant 0.585$ (see acoustic branch in figure 11*b*). It is furthermore evident from the same figure that the overall prevailing instability can come from either branch depending on the spanwise scale of the perturbation.

4.2.2. *Influence of the leading-edge Reynolds number* Re_R

The influence of the leading-edge Reynolds number Re_R on the global stability of the flow is demonstrated in figure 12. As mentioned in §2.1, variations in the leading-edge Reynolds number Re_R cause a proportional change in the sweep Reynolds number Re_s (see (2.5)). Three spanwise wavenumbers, located near the peak of the crossflow branch in figure 11(*b*) with $\beta = 0.224$ and from either side of the peak with $\beta = 0.143$ and 0.314, have been selected for this parameter study. As expected, a stabilizing effect due to a convex curvature parameterized by the leading-edge radius R has been found as Re_R is decreased from 129 136 to 32 284 (and consequently Re_s changes from 800 to 400). This observation is in accordance with wind-tunnel
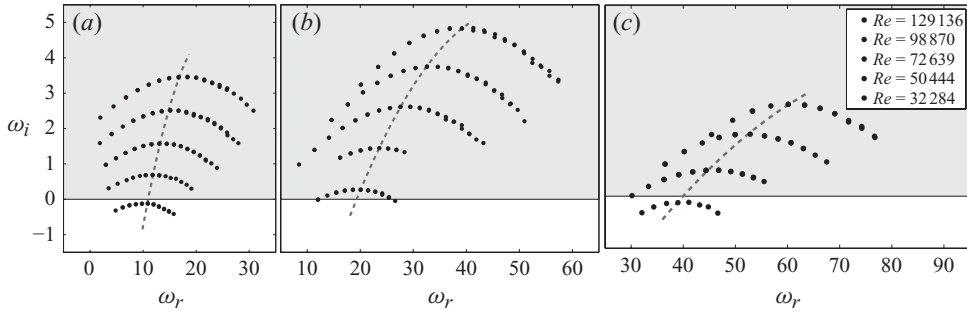
FIGURE 12. Influence of the leading-edge Reynolds number Re_R on the stability of the flow: (a) $\beta = 0.143$, (b) $\beta = 0.224$ and (c) $\beta = 0.314$. Re_R ranges from 129 136 to 32 284 (Re_s decreases from 800 to 400 with a step size of 100) from the top to the bottom. The dashed lines indicate the evolution of the maximum growth rate $\omega_{i,max}$.

experiments on a swept wing, as reported in Bippes (1999), and with theoretical studies on the effect of leading-edge curvature using local models of the attachment-line boundary layer (Lin & Malik 1997). Our results also indicate that, for the selected values of β, the frequency ω_r of the computed unstable global boundary-layer modes decreases as Re_R is decreased (see dashed lines in figure 12).

5. Summary and conclusions

The flow about yawed blunt bodies constitutes a configuration with many applications, not only in aeronautics (such as swept wings) but also in general vehicle engineering. A profound understanding of all aspects of this flow, in particular its stability characteristics, is hence important for the geometric design and analysis of any blunt body that is subject to an obliquely impinging flow.

Historically, the flow about swept bodies has been broken down into two local flow models that describe the flow in the neighbourhood of the attachment line (stagnation-point flow) and in the region further downstream (three-dimensional boundary-layer flow). Growth rates and modal structures for each of these models have been studied, and deviations from the most common assumptions, among them nonlinearities, curvature and compressibility, have been incorporated, mostly in a perturbative manner. The resulting body of literature still forms the basis for any current design process, despite the fact that discrepancies between the two local models exist. Efforts to connect the dominant structures of these two models have recently been reported (Bertolotti 1999; Mack *et al.* 2008), but a first comprehensive study of the *full* global problem has been attempted in the present study. This is possible owing to a DNS-based global stability solver, which is based on iterative algorithms and a spectral transformation of the complex eigenvalue plane (Mack & Schmid 2010*b*).

Due to the complex nature of the flow, which includes curved geometry and compressibility effects, the global spectrum is accordingly rich and intricate. Nevertheless, distinct modal structures could be identified and catalogued. Boundary-layer modes, describing the perturbation dynamics close to the wall, are dominated by structures reminiscent of crossflow vortices which connect to associated attachment-line modes. For specific parameter combinations, modes from this boundary-layer branch become unstable. Acoustic modes have been observed to fall into two categories: common wave-like structures that propagate at approximately

the respective characteristic velocities, i.e. the mean spanwise velocity plus or minus the speed of sound, and acoustic standing waves communicating between the flexible bow shock and the attachment-line region of the solid body. Symmetry properties and a hierarchy of increasingly finer spatial scales parameterize both types of acoustic modes. Wavepacket modes complete the global spectrum and describe the perturbation dynamics between the edge of the boundary layer and the bow shock. They represent the equivalent of what is known in semi- and bi-infinite flows as the continuous spectrum. Evidence supports the fact that, for our flow case, this continuous spectrum covers an area of the complex plane, rather than a curve as is the case, e.g. for classical flat-plate boundary layers.

This first attempt at extracting pertinent stability information from a complex flow in a complex geometry was aimed at dissecting the flow into physical and fundamental fluid processes that help describe the overall dynamic behaviour of infinitesimal perturbations in flow about a swept parabolic body. The role of these processes and their modification by neglected effects (specifically, nonlinearities) is an interesting and worthy topic for a subsequent investigation; it is hoped that the presented results will serve as a guide for such a study.

In general, advanced numerical techniques – both for providing highly resolved flow fields and for processing them by modern iterative algorithms – are capable of tackling the global stability problem of complex flows without the need to resort to local models or simplifying assumptions. Such a type of stability analysis, employed in this study for compressible flow about a swept parabolic body, gives a more complete and encompassing picture of the flow behaviour, and the challenge of interpreting the spectral features of the flow far outweighs the insight one gains into the global perturbation dynamics.

REFERENCES

ÅKERVIK, E., BRANDT, L., HENNINGSON, D. S., HŒPFNER, J., MARXEN, O. & SCHLATTER, P. 2006 Steady solutions of the Navier–Stokes equations by selective frequency damping. *Phys. Fluids* **18**, 068102.

BAGHERI, S., SCHLATTER, P., SCHMID, P. J. & HENNINGSON, D. S. 2009 Global stability of a jet in crossflow. *J. Fluid Mech.* **624**, 33–44.

BALAKUMAR, P. & MALIK, M. R. 1992 Discrete modes and continuous spectra in supersonic boundary layers. *J. Fluid Mech.* **239**, 631–656.

BARKLEY, D. & HENDERSON, R. D. 1996 Three-dimensional Floquet stability analysis of the wake of a circular cylinder. *J. Fluid Mech.* **322**, 215–241.

BERTOLOTTI, F. P. 1999 On the connection between cross-flow vortices and attachment-line instabilities. In *IUTAM Symposium on Laminar–Turbulent Transition, Sedona, AZ*, pp. 625–630.

BIPPES, H. 1999 Basic experiments on transition in three-dimensional boundary layers dominated by crossflow instability. *Prog. Aerosp. Sci.* **35**, 363–412.

BONFIGLI, G. & KLOKER, M. 2007 Secondary instability of crossflow vortices: validation of the stability theory by direct numerical simulation. *J. Fluid Mech.* **583**, 229–272.

GASTER, M. 1965 A simple device for preventing turbulent contamination on swept leading edges. *J. R. Aero. Soc.* **69**, 788.

GRAY, W. E. 1952 The effect of wing sweep on laminar flow. *Tech. Rep.* RAE TM Aero 255. British Royal Aircraft Establishment.

GREGORY, N., STUART, J. T. & WALKER, W. S. 1955 On the stability of three-dimensional boundary layers with application to the flow due to a rotating disc. *Phil. Trans. R. Soc. Lond.* A **248**, 155–199.

GROSCH, C. E. & SALWEN, H. 1978 The continuous spectrum of the Orr–Sommerfeld equation. Part I. The spectrum and the eigenfunctions. *J. Fluid Mech.* **87**, 33–54.

HALL, P., MALIK, M. & POLL, D. I. A. 1984 On the stability of an infinite swept attachment-line boundary layer. *Proc. R. Soc. Lond.* A **395**, 229–245.

JOSLIN, R. D. 1995 Direct simulation of evolution and control of three-dimensional instabilities in attachment-line boundary layers. *J. Fluid Mech.* **291**, 369–392.

JOSLIN, R. D. 1996 Simulation of nonlinear instabilities in an attachment-line boundary layer. *Fluid Dyn. Res.* **18**, 81–97.

KAZAKOV, A. V. 1990 Effect of surface temperature on the stability of swept attachment line boundary layer. *Fluid Dyn.* **25** (6), 875–878.

KNOLL, D. A. & KEYES, D. E. 2004 Jacobian-free Newton–Krylov methods: a survey of approaches and applications. *J. Comput. Phys.* **193** (2), 357–397.

LEHOUCQ, R. B., SORENSEN, D. C. & YANG, C. 1998 *ARPACK Users' Guide. Software, Environments and Tools: Solution of Large-Scale Eigenvalue Problems with Implicitly Restarted Arnoldi Methods.* SIAM.

LIN, R. S. & MALIK, M. R. 1995 Stability and transition in compressible attachment-line boundary-layer flow. *Tech. Rep.* 952041. SAE.

LIN, R. S. & MALIK, M. R. 1996 On the stability of attachment-line boundary layers. Part 1. The incompressible swept Hiemenz flow. *J. Fluid Mech.* **311**, 239–255.

LIN, R. S. & MALIK, M. R. 1997 On the stability of attachment-line boundary layers. Part 2. The effect of leading edge curvature. *J. Fluid Mech.* **333**, 125–137.

LIU, Y., ZAKI, T. A. & DURBIN, P. A. 2008 Boundary-layer transition by interaction of discrete and continuous modes. *J. Fluid Mech.* **604**, 199–233.

MACK, C. J. & SCHMID, P. J. 2010a Direct numerical study of hypersonic flow about a swept parabolic body. *Comput. Fluids* **39**, 1932–1943.

MACK, C. J. & SCHMID, P. J. 2010b A preconditioned Krylov technique for global hydrodynamic stability analysis of large-scale compressible flows. *J. Comput. Phys.* **229** (3), 541–560.

MACK, C. J., SCHMID, P. J. & SESTERHENN, J. L. 2008 Global stability of swept flow around a parabolic body: connecting attachment-line and crossflow modes. *J. Fluid Mech.* **611**, 205–214.

MACK, L. M. 1984 Boundary layer linear stability theory. *Tech. Rep.* 709. AGARD.

MORETTI, G. 1987 Computations of flows with shocks. *Annu. Rev. Fluid Mech.* **19**, 313–337.

OBRIST, D. & SCHMID, P. J. 2010 Algebraically decaying modes and wave packet pseudomodes in swept Hiemenz flow. *J. Fluid Mech.* **643**, 309–332.

PFENNINGER, W. 1965 Some results form the X-21 programm. Part I. Flow phenomena at the leading edge of swept wings. *Tech. Rep.* 97. AGARDograph.

POLL, D. I. A. 1979 Transition in the infinite swept attachment-line boundary layer. *Aeronaut. Q.* **30**, 607–628.

SAAD, Y., ed. 2003 *Iterative Methods for Sparse Linear Systems*, 2nd edn. Society for Industrial and Applied Mathematics.

SARIC, W. S., REED, H. L. & WHITE, E. B. 2003 Stability and transition of three-dimensional boundary layers. *Annu. Rev. Fluid Mech.* **35**, 413–440.

SEMISYNOV, A. I., FEDOROV, A. V., NOVIKOV, V. E., SEMIONOV, N. V. & KOSINOV, A. D. 2003 Stability and transition on a swept cylinder in a supersonic flow. *J. Appl. Mech. Tech. Phys.* **44**, 212–220.

SIPP, D. & LEBEDEV, A. 2007 Global stability of base and mean flows: a general approach and its applications to cylinder and open cavity flows. *J. Fluid Mech.* **593**, 333–358.

SORENSEN, D. C. 1992 Implicit application of polynomial filters in a *k*-step Arnoldi method. *SIAM J. Matrix Anal. Appl.* **13** (1), 357–385.

SPALART, P. R. 1988 Direct numerical study of leading-edge contamination. In *AGARD-CP-438*, pp. 5/1–5/13.

SPALART, P. R. 1989 Direct numerical study of crossflow instability. In *IUTAM Laminar-Turbulent Symposium III*, pp. 621–630.

THEOFILIS, V. 2003 Advances in global linear instability analysis of nonparallel and three-dimensional flows. *Prog. Aerosp. Sci.* **39**, 249–315.

TREFETHEN, L. N. 2005 Wave packet pseudomodes of variable coefficient differential operator. *Proc. R. Soc. Lond.* A **461** (2062), 3099–3122.

VAN DER VORST, H. A. 1992 Bi-CGStab: A fast and smoothly converging variation of Bi-CG for the solution of non-symmetric linear systems. *SIAM J. Sci. Stat. Comput.* **13**, 631–644.

WASSERMANN, P. & KLOKER, M. 2003 Transition mechanisms induced by travelling crossflow vortices in a three-dimensional boundary layer. *J. Fluid Mech.* **483**, 67–89.

ZAKI, T. A. & DURBIN, P. A. 2005 Mode interaction and the bypass route to transition. *J. Fluid Mech.* **531**, 85–111.